Available online at www.sciencedirect.com
SCIENCE DIRECT®
Planetary and Space Science 54 (2006) 132–143
Planetary and Space Science
www.elsevier.com/locate/pss

Low energy neutral atoms imaging of the Moon

Yoshifumi Futaana[a,*], Stas Barabash[a], Mats Holmström[a], Anil Bhardwaj[b,1]

[a]Swedish Institute of Space Physics, Box 812, SE-98128 Kiruna, Sweden
[b]NASA Marshall Space Flight Center, NSSTC/XD12, Huntsville, AL 35805, USA

Received 8 June 2004; received in revised form 7 September 2005; accepted 27 October 2005
Available online 27 December 2005

Abstract

Imaging of low-energy neutral atoms (LENAs) in the vicinity of the Moon can provide wide knowledge of the Moon from the viewpoint of plasma physics and planetary physics. At the surface of the Moon, neutral atoms are mainly generated by photon-stimulated desorption, micrometeorite vaporization and sputtering by solar wind protons. LENAs, the energetic neutral atoms with energy range of 10–500 eV, are mainly created by sputtering of solar wind particles. We have made quantitative estimates of sputtered LENAs from the Moon surface. The results indicate that LENAs can be detected by a realistic instrument and that the measurement will provide the global element maps of sputtered particles, which substantially reflect the surface composition, and the magnetic anomalies. We have also found that LENAs around dark regions, such as the permanent shadow inside craters in the pole region, can be imaged. This is because the solar wind ions can penetrate shaded regions due to their finite gyro-radius and the pressure gradient between the solar wind and the wake region. LENAs also extend our knowledge about the magnetic anomalies and associated mini-magnetosphere systems, which are the smallest magnetospheres as far as one knows. It is thought that no LENAs are generated from mini-magnetosphere regions because no solar wind may penetrate inside them. Imaging such void areas of LENAs will provide another map of lunar magnetic anomalies.
© 2005 Elsevier Ltd. All rights reserved.

Keywords: Moon; Energetic neutral atoms; Solar wind; Magnetic anomaly; Ambipolar diffusion; Space weathering

1. Introduction

Measurement of energetic neutral atoms (ENAs) is one of the good ways to monitor the interaction between plasma and neutrals remotely. ENAs are categorized by their energies: high-energy neutral atoms (HENA), medium-energy neutral atoms (MENA) and low-energy neutral atoms (LENA). HENA, MENA and LENA are ENAs in the energy ranges of 10–500 keV, 1–30 keV and 10–500 eV, respectively. Many satellites have carried ENA instruments into space to investigate the dynamics of Earth's magnetosphere and the global distributions of space plasmas (e.g. Henderson et al., 1997; Barabash et al., 1998; C:son Brandt et al., 2001).

IMAGE satellite has all three ENA imagers into the Earth's orbit. HENA imager is designed to measure ring current, inner plasma sheet and substorm injection boundary (Mitchell et al., 2000). MENA imager images the ion populations of the cusp in addition to the ring current, near-Earth plasma sheet and nightside injection boundary (Pollock et al., 2000). Primary role of LENA instrument is to image the outflow of low-energy ions from the auroral ionosphere (Moore et al., 2000).

Cassini is the first satellite with ENA instrument to another planet. On its way to Saturn it unexpectedly revealed that Europa generated a gas cloud comparable in gas content to that associated with the volcanic Io (Mauk et al., 2003). Mars Express also carries an ENA instrument to Mars to monitor hydrogen and oxygen ENAs (Barabash et al., 2002). In near future, ENA instruments are planned to fly to Venus on Venus Express mission, to the Moon on Chandrayaan-1 mission (Bhardwaj et al., in press), and to Mercury on Bepi-Colombo mission (Barabash et al., 2001).

*Corresponding author. Tel.: +46 980 79025; fax: +46 980 79050.
E-mail address: futaana@irf.se (Y. Futaana).
[1]On leave from Space Physics Laboratory, Vikram Sarabhai Space Centre, Trivandrum 695022, India.

0032-0633/$ - see front matter © 2005 Elsevier Ltd. All rights reserved.
doi:10.1016/j.pss.2005.10.010

Investigation of the lunar surface composition by sputtered particles has been proposed by measuring ionized particles with mass-spectrometer (Managadze and Sagdeev, 1988; Elphic et al., 1991). This is the analogous approach to the secondary ion mass spectrometry, the standard laboratory surface composition analysis technique. Hilchenbach et al. (1991) analyzed data obtained by a time-of-flight spectrometer SULEICA on the AMPTE/IRM satellite and detected heavy ions with the mass range between 23 and 37 amu. Mall et al. (1998) analyzed lunar-originated heavy ions by STICS on the WIND spacecraft during its 17 lunar flybys and detected the ion species of O^+, Al^+, Si^+, and P^+. However it is difficult to map those elements to the lunar surface because the observations are far from the Moon and ionized particles have complicate trajectories in the vicinity of the Moon and in the space. The ionized particles feel large Coulomb force and Lorenz force, and hence they are easily diffused or reflected by electromagnetic instabilities or small-scale magnetic fields of lunar surface origin (Lin et al., 1998; Futaana et al., 2003).

The LENAs can be generated from the surface with tenuous atmosphere such as Mercury and the Moon. The LENAs generated at the surface of the Moon are not bound by the gravity potential since the escape energy at the Moon is ~2.4 km/s (1.7 eV even for Fe). Therefore the LENAs are not the source of the exospheric particles. Even their trajectories are modified by small gravity potential, they go almost straight with its initial velocity. Imaging of sputtered LENAs is a much better technique to map lunar surface elements than the charged-particle mass spectrometry.

Close distance LENA imaging may also provide information on the magnetic anomalies. The Moon has no global magnetic field but there are many locally magnetized regions on the surface. Their typical spatial scale is several 100 km, and the strength at the surface is on the order of ~100 nT. They are widely distributed at the lunar surface but large anomalies are believed to be located at the antipodes of large craters. The generation mechanism of such large anomalies has been an open question. Another question is that some specific albedo structures exist very close to the strongly magnetized regions (Hood et al., 1979; Richmond et al., 2003). One possible explanation is that the magnetized regions can deflect the solar wind precipitation for long time, so that the weathering of the lunar surface materials inside the magnetized regions is slower than that outside of them.

This structure must affect the LENA generation. Therefore, imaging the LENAs should reflect the difference in the precipitating flux of the solar wind around the magnetic anomalies. The sputtering and the weathering processes are closely related to the generation mechanisms of LENAs, and therefore imaging of LENAs will give us information on these important issues of lunar science.

For LENA imaging we have to note that the light-shadowed regions and the LENA-shadowed regions are different because of the following two reasons. The first reason is the finite gyro-radius effect of the solar wind with finite thermal velocity and hence the solar wind particles have helical trajectories. The second reason is the pressure gradient and the electric potential between the solar wind region and the vacuum region behind the Moon (Colburn et al., 1967; Ogilvie et al., 1996; Birch and Chapman, 2001; Futaana et al., 2001). Because of these two reasons, LENA imaging can provide information about the permanent light-shadowed area. For example, we might be able to detect the water in the polar region of the lunar surface since a part of solar wind particles may reach this shadowed region. The current LENA instrument does not have enough mass and angular resolution to differentiate between oxygen ($M = 16$) and water molecules ($M = 18$) (Kazama et al., in press), but it may be fundamentally possible to distinguish them in the future with more advanced instrumentation.

In this paper, we examine expected images of LENAs by satellite-based measurements around the Moon. Physical topics related to the Moon surface which might be relevant for LENA imaging are introduced and discussed. In Section 2, properties of the LENA production at the lunar surface are formulated. In Section 3, model calculations are made for LENA-related topics in the vicinity of the Moon. Section 4 is a summary and conclusions.

2. LENA production

2.1. Sputtering process

Since the Moon has no global magnetosphere and no significant atmosphere, LENAs are generated mainly from sputtering by precipitating ions, photon stimulated desorption (PSD) and micrometeorite vaporization. The vaporization produces atoms with a Maxwell distribution with an average gas temperature of 4000 K (= 0.34 eV) (Wurz and Lammer, 2003) and this is below the lower energy limit of LENA instruments (~10 eV). Atoms generated by PSD have an energy spectrum of $f(E) \sim E^{-(\beta+1)}$, where β varies from 0.25 to 0.7 (Johnson et al., 2002b). These atoms have energies mainly around the binding energy (typically 2–4 eV (Wurz and Lammer, 2003)). Since particles with energies larger than 10 eV have never been observed, we exclude the PSD as a generation mechanism of LENAs, and then consider only sputtering by solar wind particles in this study.

The energy spectrum of the sputtered particles, $f(E)$, is formulated by the Thompson–Sigmund formula (Thompson, 1968; Sigmund, 1969)

$$f(E) = C \frac{nE}{(E+E_b)^3}\left(1 - \sqrt{\frac{E+E_b}{E_i}}\right), \quad (1)$$

where E is the sputtered particle energy, n is the particle density, E_b is the surface binding energy of 2–4 eV (Wurz

and Lammer, 2003), E_i is the energy of precipitating charged particles, and $C = 2E_b/4\pi$. The spectrum has the cut-off energy, $(E_i - E_b)$. This spectrum is confirmed for the extremely low energy range (Betz and Wien, 1994). Betz and Wien (1994) modified the Thompson–Sigmund formula to consider the mass of the impinging and sputtered atoms:

$$f(E) = C' \frac{nE}{(E+E_b)^3}\left(1 - \sqrt{\frac{E+E_b}{E_i'}}\right), \quad (2)$$

where E_i' is defined as

$$E_i' = 4E_i \frac{M_1 M_2}{(M_1+M_2)^2}, \quad (3)$$

where M_1 and M_2 is the mass of impinging and sputtered species, respectively. The spectrum has the cut-off energy $E_{co} = E_i' - E_b$. The coefficient C' is the normalize factor of the spectrum to satisfy $\int f(E)\,dE = n$. As calculated in Fig. 1 (Section 2.3), there is a significant flux of sputtered atoms in the energy range (>10 eV) which exceeds escape energy and the gravitational binding of the trajectories, making LENA imaging of the precipitation regions possible.

The only loss mechanism of LENAs of the Moon is photoionization. The time scale of photoionization is long enough to make LENA imaging valuable in space. For example, Potassium has the shortest ionization time ($\sim 7.5 \times 10^4$ s) among species which are known to exist around the Moon. Thus LENA imaging by an instrument on board a lunar orbitor (many of lunar orbitors are located at a height of $\sim$100 km) is a viable method to investigate the sputtered particles.

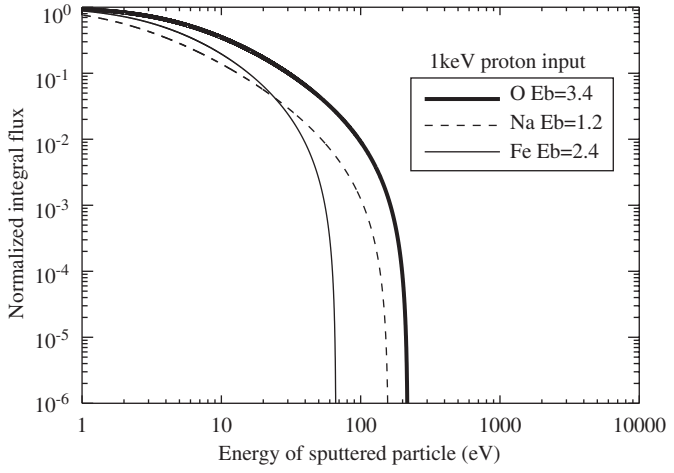

Fig. 1. Normalized energy spectrum of the sputtered products derived from Eq. (4). The distribution function shown in (2) is used. O (thick), Na (broken), and Fe (solid) are examined. The binding energies are taken from Wurz and Lammer (2003).

2.2. Precipitating particles

The Moon is mainly located in the solar wind. It is exposed in the solar wind for about 80% of its orbit under the typical magnetosphere size of the Earth. The typical bulk energy of the solar wind proton is 0.5–2 keV and the temperature is much lower, typically 10 eV. Therefore, the solar wind flux can be considered as an ion beam source.

The yields of the sputtered particles depend on the energy and the species of impinging particles. Examples of the energy dependency can be found in Johnson (1990) and references therein. Fig. 3.16 in Johnson (1990) shows that the dependency in the energy range 0.5–2 keV is within one order in case of proton injection. The energy dependency is taken into account in the following model.

The impinging species is also the key of the sputtered particle flux. We modeled only the solar wind proton as precipitation particles in the following for simplicity, because typical solar wind particles consist of $\sim$95% of H^+ and $\sim$5% of He^{++}. Solar wind He^{++} particles have larger energy and mass than H^+, so that the yield is expected to be larger (Johnson and Baragiola, 1991) and the energy distribution of sputtered particles will have more flux in the higher energy range. Hence, taking the He^{++} particles into consideration, the flux of sputtered particles is expected to be higher.

2.3. LENA flux

As soon as the ion precipitation flux is known, the integrated sputtered LENA flux with energy larger than E_0, $\Phi_{LENA}(E > E_0)$, can be estimated by

$$\Phi_{LENA}(E > E_0) \sim \frac{1}{2\pi} g(E_0) Y(E_{ion}) S \Phi_{ion}(E_{ion}), \quad (4)$$

$$g(E_0) = \frac{\int_{E_0}^{E_{co}} f(E)\,dE}{\int_0^{E_{co}} f(E)\,dE}. \quad (5)$$

$Y(E_{ion})$ is the particle yield from the surface for the incident ion beam of energy E_{ion}, S the abundance of the atoms of interest in the lunar regolith, $\Phi_{ion}(E_{ion})$ is the precipitating ion flux integrated over an energy band around E_{ion}. $g(E_0)$ is the normalized energy spectrum of the sputtered products calculated by means of Eq. (2). The function $g(E_0)$ for three different elements (O, Na and Fe) are displayed in Fig. 1. We used the binding energies of 3.4, 1.2 and 2.4 eV for O, Na and Fe, respectively (Wurz and Lammer, 2003).

2.4. Sputtered particles

We can estimate the sputtered lunar LENA flux from previous studies. Parameters used in this estimation are shown in Table 1. Abundance for each species is from Morgan and Killen (1997). Lammer et al. (2003) estimated the O, Na and Ca yields sputtered by an H^+ beam, which is

Table 1
Mass, abundance in relative number, binding energy, and yield for main elements of the Moon

Elements	Mass	Abundance in number	Binding energy (eV)	Yield Min (500 eV H+)	Yield Max (2 keV H+)
O	16	0.6	3.4	**0.025**	**0.04**
Si	28	0.16	2.4	0.025	0.082
Al	27	0.1	2.4	0.025	0.082
Mg	24	0.05	2.4	0.025	0.082
Ca	40	0.05	2.1	**0.032**	**0.06**
Fe	56	0.025	2.4	0.025	0.082
Na	23	0.004	1.2	**0.037**	**0.082**
Other	—	0.011	—	—	—

Values of abundance are taken from Morgan and Killen (1997). Values of the binding energy are taken from Wurz and Lammer (2003). Minimum and maximum of the yield corresponds to the impinging proton energy with 500 eV and 2 keV, respectively. Yields given in bold is taken from Lammer et al. (2003) and yields for the other elements are for that of O (min) and Na (max).

Table 2
Cutoff energy, ratios of the numbers of sputtered particles with energies larger than 10 and 100 eV to numbers of sputtered particles, estimated LENA flux for various lunar elements using the Eq. (2)

	Cutoff energy (E_{co} (eV))	g ($E>10$ eV)	g ($E>100$ eV)	Min flux $E>10$ eV (/cm^2 s sr)	Max flux $E>10$ eV (/cm^2 s sr)	Min flux $E>100$ eV (/cm^2 s sr)	Max flux $E>100$ eV (/cm^2 s sr)
O	218	0.35	0.0092	2.5×10^5	4.0×10^5	6.6×10^3	1.1×10^4
Si	131	0.24	0.0010	4.6×10^4	1.5×10^5	2.0×10^2	6.5×10^2
Al	135	0.25	0.0013	2.9×10^4	9.6×10^4	1.5×10^2	5.0×10^2
Mg	151	0.251	0.0022	1.5×10^4	4.9×10^4	1.3×10^2	4.4×10^2
Ca	93.1	0.197	0.000	1.5×10^4	2.8×10^4	0	0
Fe	66.5	0.195	0.000	5.8×10^3	1.9×10^4	0	0
Na	159	0.138	0.0012	9.8×10^2	2.2×10^3	8.5×10^0	1.9×10^1

We assumed 1 keV proton input to calculate E_{co} and $g(E)$. Parameters used in the estimation are shown in Table 1.

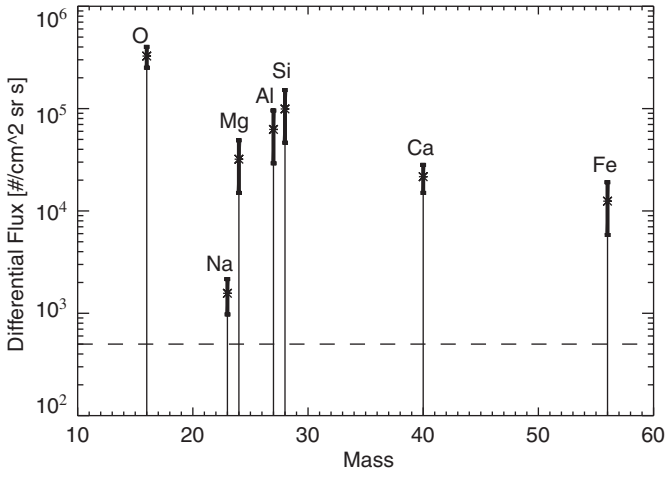

Fig. 2. Expected differential flux for each element with energies larger than 10 eV. The dashed line at 500 (/cm^2 sr s) corresponds to the one-count level of the LENA imager suggested by Kazama et al. (in press).

emphasized in bold. The minimum and maximum yield in the table corresponds to impinging particle energies of 0.5 and 2.0 keV, respectively. The results are summarized in Table 2. The sputtered LENAs in the energy range of >10 eV are 2–4 $\times 10^5$/cm^2 sr s for O, 0.1–1 $\times 10^5$/cm^2 sr s for Ca, Si, Al, or Mg, and 0.1–2 $\times 10^4$/cm^2 sr s for Fe or Na.

Fig. 2 shows the differential flux of each element with energies higher than 10 eV with respect to mass. The dashed line at 500 (/cm^2 sr s) is the differential flux corresponding to the 1 count (one-count level) of the LENA imager proposed in Kazama et al. (in press). The imager has geometric factor $G\sim5$ cm^2 eV/channel for the energy channel centered at 25 eV, efficiency of $e=1\%$ and $dE/E=1$ (FWHM). The one-count level of this energy channel is calculated by dE/eG. Note that most of the generated LENA has energy between 10–50 eV (Fig. 1), which is covered by this energy channel. The result shows that all major elements can be imaged by the imager, and thus we can obtain the global elemental maps of sputtered particles by global LENA imaging.

2.5. Discussion on LENA flux

The LENA fluxes of the Moon are estimated in the previous section. We discuss the estimation by comparing previous studies of exospheres of the Moon and other solar system bodies.

Wiens et al. (1997) discussed the sodium ion cloud in the vicinity of Io, and concluded that the theoretical

Thompson–Sigmund distribution is a good approximation for the energy distribution of the Na ejected by the sputtering of the energetic heavy ions from the laboratory experience. Johnson et al. (2002a) investigated the Europa's sodium atmosphere and concluded that the Thompson–Sigmund formulation can well explain the sputtered sodium from the Europa's surface. These results suggest that the energy distribution assumed in this paper (Eq. (2)) can be applied to the energy distribution of sputtered LENAs from the lunar surface.

We used the yield values calculated by Lammer et al. (2003) to estimate the LENA fluxes. The calculation is based on the linear collision cascade theory, then the yield values adopted can cause the overestimation of the LENA flux. In addition, when we apply laboratory sputtering yields to a satellite observations, we might also need to consider the reduction of the flux due to porosity of the regolith (factor ~4) (Johnson, 1989; Johnson, 2000). Therefore our theoretical estimation in Table 2 (e.g. $(2–4)\times10^5/\mathrm{cm^2\,s\,sr}$, for oxygen) could be overestimated, but not by more than one order of magnitude.

Let us compare with the past optical observations of the exospheric particles. The estimated flux of oxygen atoms with energy $>10\,\mathrm{eV}$ (35% of all the sputtered oxygen) implies that $\sim(0.7–1.1)\times10^6\,\mathrm{atoms/cm^2\,s\,sr}$ are sputtered. If we take typical velocity ~4.4 km/s (~1.6 eV, corresponding to the energy of the peak of the spectrum (2)), the density is estimated to be $10–16/\mathrm{cm^3}$. This value is within the upper limit of $500/\mathrm{cm^3}$ set by the Apollo 17's UV spectrometer (Feldman and Morrison, 1991).

There are several ground-based observations and simulations about sodium exosphere of the Moon (Potter and Morgan, 1988; Sprague et al., 1992; Flynn and Mendillo, 1995). Their conclusions are that 7×10^4 (Potter and Morgan, 1988), 12×10^4 (Sprague et al., 1992), and 2×10^4 (Flynn and Mendillo, 1995) sodium atoms are generated. Flynn and Mendillo (1995) describes that sodium atoms are generated by the micrometeoroid vaporization, thermal desorption, photon-stimulation desorption and sputtering. From our estimation $((1–2)\times10^3/\mathrm{cm^2\,s\,sr}$ of sputtered sodium atoms with energy larger than 10 eV), ~4–10× $10^4/\mathrm{cm^2\,s\,sr}$ sodium atoms in all energy range are sputtered by solar wind protons. The estimated flux of sodium is within the same order of the previous observations. Although our estimation might be overestimated because there are other mechanisms that can create sodium atoms, the difference should not be more than the order of magnitude. Note that the calculated flux of the oxygen LENAs are significantly higher by three orders of magnitude than the one-count level of existing instrument $(500/\mathrm{cm^2\,s\,sr})$. Therefore, the LENAs from the lunar surface can be detected by the LENA imager.

3. LENA imaging of the Moon

In this section, we study three subjects where a LENA instrument can contribute to the lunar science. First we study the general sputtering, i.e., sputtering from the dayside surface for element mapping study. Next, we consider shadowed regions, where solar wind particles can reach due to the finite gyro-radius effects and pressure gradients. This means that solar wind terminators can be defined differently from the optical terminator, the day–night boundary. We also consider a permanently shadowed crater. Then we examine whether we can detect magnetic anomalies by LENA imaging.

3.1. Imaging of LENA

For tightly-bound solids, the generation of sputtered LENAs is proportional to the elastic energy transferred by the incident solar wind particle to target atoms near the surface. The relative yield of different elements reflects the surface composition. LENA imaging will thus provide maps of the sputtered elements, which fundamentally reflect the surface composition.

Fig. 3(a) shows the solar wind precipitation in a latitude–longitude map of the Moon. Because the thermal velocity of the solar wind is not taken into account in this model, the precipitating solar wind flux is just proportional to $\cos\chi$, where χ is the solar zenith angle. The thermal velocity affects only the region of large χ, and this effect is treated in the later section.

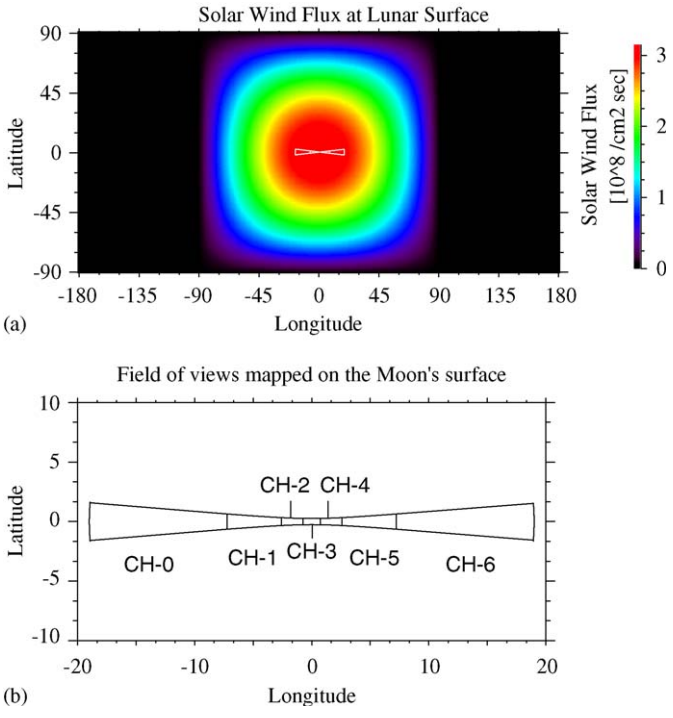

Fig. 3. (a) The model of the solar wind precipitating flux at the lunar surface. Here, we take the typical solar wind density as $7/\mathrm{cm^3}$ and the typical bulk velocity as 450 km/s. The origin of the longitude is the sub-solar point. The flux is assumed to depend only on the solar zenith angle. White rectangles show the field of views mapped on the lunar surface. (b) The zoomed-in view near the sub-solar point. Each rectangle corresponds to the instrumental field of view mapped on the lunar surface.

The LENA instrument used throughout this paper is assumed to have 7 channels (CH) with field of view of $9^\circ \times 25^\circ$ for each (Kazama et al., in press). The trajectory of a satellite carrying the instrument is assumed to be a circular orbit with a height of 100 km (Bhardwaj et al., in press). The white rectangles in Fig. 3(a) at the subsolar point is the instrumental field of view mapped on the lunar surface. Fig. 3(b) depicts the magnification. The intrinsic field of view of 25° corresponds to 1.46° (44 km) at the surface for CH-3, the channel looking nadir. Thus LENA imaging can provide maps with spatial resolution of ~50 km for the lunar sputtered materials.

Fig. 4 shows an image of the number of sputtered oxygen atoms from the lunar surface. The differential flux for each channel, J_i, can be calculated as

$$J_i = \frac{1}{2\pi\omega_i}\int_{\Omega_i} f_{SW} A\, Y g(E)\, d\Omega_i, \quad (6)$$

where Ω_i covers the solid angle of the instrumental field of view for ith channel depending on the location and the attitude of the instrument, ω_i is the intrinsic solid angle for ith channel, f_{SW} is the solar wind flux, A is the abundance of oxygen, Y is the yield, and $g(E)$ is the ratio of sputtered oxygen with energies larger than E relative to all of the sputtered oxygen atoms formulated in Eq. (5). We take the lower threshold energy E as 10 eV and $g(E)$ as 0.36 for oxygen (Table 2). Also from Table 1, $A = 0.6$ and $Y = 0.0315$ by averaging maximum and minimum yields. The sputtered particles are assumed to be ejected isotropically.

For all channels, the expected oxygen flux is well above the one count level of 500 ($/cm^2$ sr s) for the real instrument. The flux in CH-0 is higher than that in CH-3. This is because the area covered by the field of view in CH-0 is much larger than CH-3 (Fig. 3(b)).

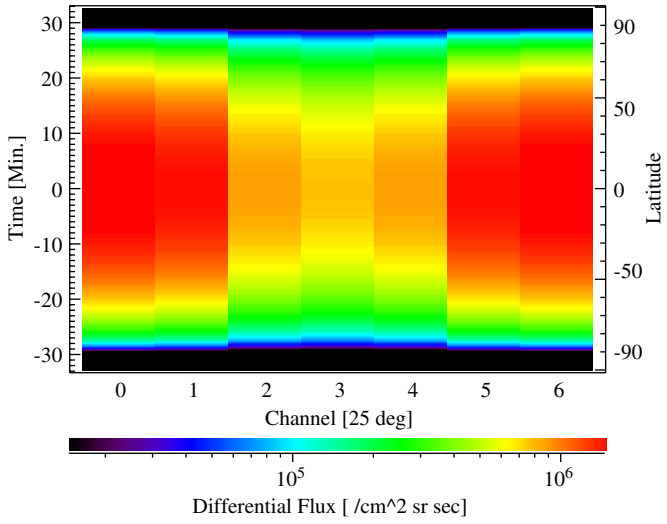

Fig. 4. Calculated oxygen LENA image along the trajectory of satellite, that is assumed to be a circular orbit with height of 100 km in the plane of Sun–Moon meridian. Each channel is assumed to have intrinsic field of view of $9^\circ \times 25^\circ$.

We can also infer the differential fluxes for other elements. Relative richness of the other elements to the oxygen are the same as shown in Table 2 or in Fig. 2. The differential flux for Mg, Al, Si, Ca and Fe is about an order of magnitude less than that of O, and the expected flux at the instrument position is also one order less, i.e. 10^4-10^5 ($/cm^2$ sr s), but well above the one-count level. Na, with differential flux two orders of magnitude less than that of O, is also above the one-count level with the expected differential flux of $\sim(1-2)\times 10^3$ ($/cm^2$ sr s).

The above calculations do not include finite gyro-radius effects, pressure gradients formed around the wake region, and electric potentials (Ogilvie et al., 1996; Futaana et al., 2001). This is why we do not have any counts from the darkside hemisphere. When these effects are taken into account, we expect some fluxes from the darkside as discussed in a later section.

Although we assumed isotropic ejection from surface for the LENA flux estimation, the real ejection is expected to be anisotropic with respect to the surface normal. This anisotropy might increase the flux close to the surface normal direction (Betz and Wien, 1994). Therefore it will not affect the detectability by the LENA instrument above the surface which is looking in nadir direction. However, at present we do not know how much the flux would decrease in the oblique direction.

Another factor that might reduce the flux is surface roughness. Reduction of the flux for the real regolith is factor of 0.4–1 according to Johnson (1989), and this does not affect the LENA detectability. Therefore we do not consider this effect.

The capability of LENA imaging of different elements as shown in Fig. 2 allows us to obtain global imaging on the surface elemental composition. Sputtered neutral atoms have good stoichiometry (Johnson and Baragiola, 1991), so basically these images can be converted to the chemical composition map. There exist some difficulties due to complications of the lunar surface conditions, ambiguity in theories, or limitation of LENA imaging due to its mass or energy resolution. However, using complementary observations by other imaging techniques, LENA imaging can fundamentally be converted to the chemical composition map of the Moon.

3.2. Imaging of shadowed areas

Unlike the photon, the solar wind protons have a thermal velocity and their trajectories are twisted by the electric field, so that some solar wind protons can reach permanently shadowed areas. Imaging the LENAs generated in such areas will give us information related to the surface composition there. The observations in the shadowed region have an advantage of reducing contamination due to the solar UV. Another advantage in imaging the permanently shaded region is that we might be able to detect frozen materials such as water if we can have a

LENA imager with good mass and angular resolution in the future.

3.2.1. Solar wind plasma terminator

The Moon is an obstacle to the solar wind flux and a void region is generated behind the Moon since the solar wind is a supersonic flow. The solar wind flowing past the terminator is accelerated by a pressure gradient, i.e. its thermal velocity, along the magnetic field lines and penetrate into the void region. The solar wind terminator, the boundary which separate the regions where the solar wind ions can reach or not, can be formed behind the terminator, and LENAs can be generated on the light-shadowed area between the terminator and the solar wind terminator.

To investigate the solar wind terminator, we used a two-dimensional model that treats the plane containing the magnetic field and the solar wind flow. A sketch of the configuration is drawn in Fig. 5. For simplicity, the solar wind magnetic field is assumed to be perpendicular to the solar wind flow vector for the simplicity. The coordinate system used in this formulation is as follows: the x-axis is taken as the direction of the solar wind flow vector and the y-axis as the direction of the magnetic field. The origin is the lunar center. The solar wind flow connects the x-coordinate and the time past the terminator (t) through $x = -V_{sw}\,t$, where V_{sw} is the velocity of the solar wind. The physics along the magnetic field direction is described by a general theory of ambipolar diffusion. Then we apply one-dimensional theory on this diffusion process.

From a two-fluid point of view, the solar wind electrons tend to penetrate into the void region faster than the protons because of their light mass, and the resulting charge separation will accelerate the protons and decelerate the foregoing electrons. It is a morphological view of the ambipolar diffusion.

The temporal and spatial scale of the charge separation is related to the electron plasma frequency (typically 10 kHz) and the Debye length (typically 20 m), respectively. When we treat plasma phenomena on a lunar global-scale which is typically 1000 km, such a microscopic view can be simplified with the MHD approximation.

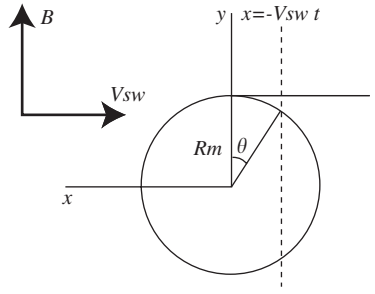

Fig. 5. The geometry to derive the solar wind plasma terminator. x- and y-axis is determined as the direction from the Moon to the Sun and the direction of the magnetic field, respectively. x coordinates can be connected to the time (t) by the solar wind velocity V_{sw}. θ is the angle behind the terminator.

This is a classical view for plasma diffusion into the void region (for example, see review by Samir et al. (1983)). Here we used the one-dimensional (ζ-axis) two-fluid model with the initial condition ($t = 0$; corresponding to the terminator) that the undisturbed plasma with constant density N_0 exists only in $\zeta > 0$ (corresponding to the undisturbed solar wind) and there are no plasma in $\zeta < 0$ (corresponding to the void region). The charge-neutral two-fluid theory results in density and velocity of the ions as

$$N_i(\zeta) = N_0 \exp\left[-\left(\frac{\zeta}{S_0 t} + 1\right)\right] \tag{7}$$

and

$$V_i(\zeta) = S_0\left(\frac{\zeta}{S_0 t} + 1\right), \tag{8}$$

respectively. Here S_0 ($= \sqrt{\gamma k_B T_e / m_i}$, where γ is the ratio of specific heat, k_B is the Boltzmann constant, T_e is the electron temperature, and m_i is the ion mass) is the ion acoustic speed of the solar wind (e.g. Baumjohann and Treumann, 1997). The solution is valid for $t > 0$ and $\zeta > -S_0 t$.

We have made some assumptions for the development of our theory. The floating potential of the Moon relative to the interplanetary space is neglected. The Moon's surface is assumed to be transparent to the plasma for simplicity. This assumption ignores the effect by the direct interaction between the plasma and the lunar surface, which is a complicated process. We also ignore the sputtered charged particles which are expected to be too few to affect the physics.

The penetrating solar wind density and velocity at a specific y is expressed by

$$N = N_0 \exp\left(\frac{y - Rm}{S_0 t} - 1\right), \tag{9}$$

$$V_y = S_0\left(\frac{y - Rm}{S_0 t} - 1\right), \tag{10}$$

from Eqs. (7) and (8). Here, N_0 is the undisturbed solar wind density. and Rm is the lunar radius. The plasmas also have the velocity perpendicular to the magnetic field direction:

$$V_x = -V_{sw}. \tag{11}$$

Here x, y and t can be expressed by the angle behind the terminator (θ):

$$x = -Rm \sin\theta, \tag{12}$$

$$y = Rm \cos\theta \tag{13}$$

and

$$t = -\frac{x}{V_{sw}} = \frac{Rm}{V_{sw}} \sin\theta. \tag{14}$$

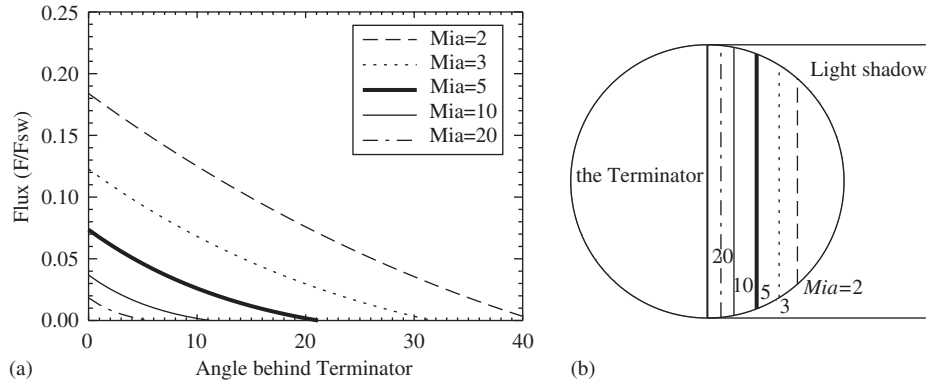

Fig. 6. Results of two-fluid 2-D model calculation of solar wind terminator. (a) Solar wind flux at the lunar surface behind the terminator for ion-acoustic Mach numbers $M_{IA} = 2$ (dashed), 3 (dotted), 5 (thick), 10 (solid) and 20 (dot-dashed). (b) Solar wind terminator for various Mach numbers.

The flux, F, can be calculated by a general equation

$$F = -N\vec{v} \cdot \vec{r}, \tag{15}$$

where $\vec{r}$ is a normal vector of the surface, i.e., $r_x = \sin\theta$ and $r_y = \cos\theta$.

Substituting Eqs. (9)–(14) into (15), we obtain a general expression for the normalized solar wind flux behind the Moon as

$$\frac{F}{f_{sw}} = \frac{1}{M_{IA}}\cos\theta\left(1 - M_{IA}\frac{\sin\theta}{\cos\theta(1+\cos\theta)}\right) \times \exp\left(-1 - M_{IA}\frac{\sin\theta}{1+\cos\theta}\right), \tag{16}$$

where $M_{IA} = V_{sw}/S_0$ is the ion-acoustic Mach number. Eq. (16) indicates that the normalized flux is controlled only by the parameter M_{IA}.

Fig. 6(a) displays the precipitating flux behind the terminator, normalized by the upstream solar wind flux. The flux decreases as the ion-acoustic Mach number increases, which makes sense. For a nominal value of $M_{IA} = 10$ for the solar wind, the flux at the terminator is ~4% of the upstream solar wind flux and the yield of LENAs is expected to be 4% of the sub-solar point value. The flux can also reach ~10° behind the Moon. Fig. 6(b) shows the solar wind terminator, the boundary where the solar wind can reach, for various Mach numbers. This fact means that the solar wind terminators for the unmagnetized body are far different from the terminator of sun light and LENA imaging is possible at the surface behind the terminator.

At around the boundary between the solar wind and the void, relatively large negative electric potentials of ~400–500 V have been indicated by Ogilvie et al. (1996) and Futaana et al. (2001) by different methods, although the generation mechanism is not well-known. The solar wind protons can be further accelerated and the flux increased compared to the above result by such a large negative electric potential.

3.2.2. *Permanently shadowed craters*

It is believed that there are permanently shadowed areas on crater rims at latitude higher than 78° (e.g. Bussey et al., 2003). These permanently shadowed areas might conserve water materials delivered by various processes on planetologically significant time periods. Arnold (1979) estimated that the total of $\sim 10^{10}-10^{11}$ tons of H_2O are delivered by comets, meteoroids and interplanetary dust particles. Feldman et al. (1998) argued the existence of the water ice at both of the poles using the data from epithermal neutron flux by Lunar Prospector. Feldman et al. (2000) concluded that at most 2.05×10^9 tons of water can be deposited at both poles of the Moon. Crider and Vondrak (2003) suggested that solar wind can supply H-species in the polar regions at a level comparable to that observed by Lunar Prospector.

Even though the sun light cannot reach the shadowed craters, the solar wind particles are capable of reaching there because the solar wind particles have the finite gyro-radius due to their thermal velocity, and they move helically around the interplanetary magnetic field (IMF). The finite gyro-radius effect is important around the polar region. We calculated trajectories of solar wind protons to assess how a shadowed crater is illuminated by the solar wind.

The upper panel of Fig. 7 shows the geometry. The gray area in this panel is the body of the Moon with the crater at the pole. A permanently shadowed crater is modeled by a parabolic curve with depth of 2 km and the radius of 10 km at the pole. The solar wind particles are modeled by 5,000,000 test particles with bulk velocity of 400 km/s ($-x$-axis) and isotropic thermal velocity of 70 km/s. The IMF is assumed to be perpendicular (y-axis) to the solar wind velocity and the magnitude is 5 nT. Filled symbols at the lunar surface denote the locations where test particles impact to the lunar body. We have selected 1/15 of all test particles to make this plot.

Lower panel of Fig. 7 shows the flux of the solar wind protons. The result is normalized by the solar wind flux (F_{sw}). The average solar wind flux at the polar region due

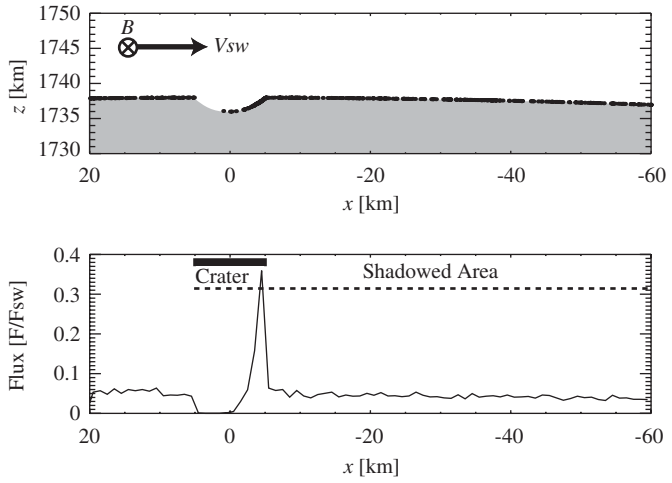

Fig. 7. (Upper) Locations of place where the solar wind proton precipitates onto the Moon surface. A crater is modeled by a parabolic curve with the depth of 2 km and the radius of 10 km. Each filled circle denotes the location where a test particle impacts at the lunar surface. (Lower) Solar wind flux reaching at the lunar surface as a function of the distance from the terminator of the Moon. The number of the test particles is normalized by the solar wind flux.

to the finite gyro-radius effect is ~5%. The resulting sputtered oxygen flux is estimated to be (1.2–2.0)× 10^4/cm^2 s sr, which is high enough for detection by the existing LENA instrument. While no solar wind protons precipitate in the front half of the crater ($x>0$), we expect high illumination by solar wind in the region x~2–5 km behind the bottom as shown in Fig. 7. This means that the permanent-shadowed regions are not the permanent solar wind shadow. The solar wind impinging flux can be changed by factor of 5 due to the geometry of the surface, and hence precise geometrical measurements are necessary to analyze and to interpret the LENA imaging. Actually, the estimated fluxes depend highly on the shape and the size of the craters.

To investigate polar-shadowed regions precisely, the angular resolution of the LENA instrument needs to be improved. As shown in Fig. 3(b), the best angular resolution at the surface is ~44 km, which is ~1–2 order coarser to study the shadowed area.

It should also be noted that electron kinetics might play a role as well as ion kinetics in this region. The gyro-radius of the solar wind electrons with a typical temperature of 10 eV and typical magnetic field of 5 nT is about 3.5 km, which is comparable to the scale of a typical crater at the Moon.

3.3. Imaging of magnetic anomalies

Imaging of LENA has possibilities to improve our knowledge about the interaction between the magnetic anomalies and the solar wind. The interaction may create the smallest known magnetosphere, magnetosheath and bow shock systems in the solar system (Lin et al., 1998).

Russell and Lichtenstein (1975) statistically showed the existence of limb compressions, which is the magnetic field enhancement appearing only in specific selenographic regions, and the occurrence is correlated with the surface magnetic field strength. They concluded that the most probable cause of limb compressions is the deflection of the solar wind by the lunar surface magnetic anomalies in the limb region. However, it has been believed that the lunar magnetic field was too weak to repel the charged solar wind.

Lunar Prospector's in situ observations found magnetic anomalies on the lunar surface that can stand off the solar wind (Lin et al., 1998). They claimed that the solar wind cannot reach inside the mini-magnetosphere. One of the most controversial issues is that the spatial size of the magnetic anomalies (of the order of 100 km) is comparable to that of the solar wind ion gyro-radius (typically 30–150 km). Kinetic effects due to the finite gyro-radius of the solar wind ion might be important under this condition.

There are a few simulations on the interaction between the solar wind and magnetic anomalies. Hood and Williams (1989) used test particles to consider the deflection effect at around the magnetic anomalies, but their interest was limited only to the region very close to the magnetic anomalies and no kinetic effects were included. Harnett and Winglee (2002) compared the MHD simulations and particle simulations and found that large anomalies are capable of forming the magnetosphere, i.e. the solar wind void regions.

These observations and simulations imply that the formation of void regions could be possible although the solid theory of the formation of the small-scale solar wind void has not been established yet. LENA imaging can provide new aspects about the study of the interaction between the magnetic anomalies and the solar wind. The depletion of the LENA flux at around the magnetized regions, if observed, is the evidence for the formation of the mini-magnetosphere.

We calculated expected LENA images seen from an orbitor at height of 100 km in the Sun–Moon meridian together with the solar wind precipitating flux for some simple anomaly models to consider whether LENA depletions can be seen or not when the solar wind void is formed. The sputtered LENA flux is expected to disappear in such void region. The question is whether the LENA instrument can detect such a change of the LENA flux. Two cases are examined: modeled void region with the radius of 100 km (~3.3°) located at (a) the sub-solar point and (b) at $\lambda = 5°$ and $\phi = 5°$, where λ and ϕ is the local latitude and longitude measured from the sub-solar point.

Fig. 8 displays the results of the simulation. The upper panels show the solar wind precipitating maps projected onto the lunar surface and the middle panels show the images of LENA imager in the same format as Fig. 4. The lower panels show the time series of the differential flux for each channels.

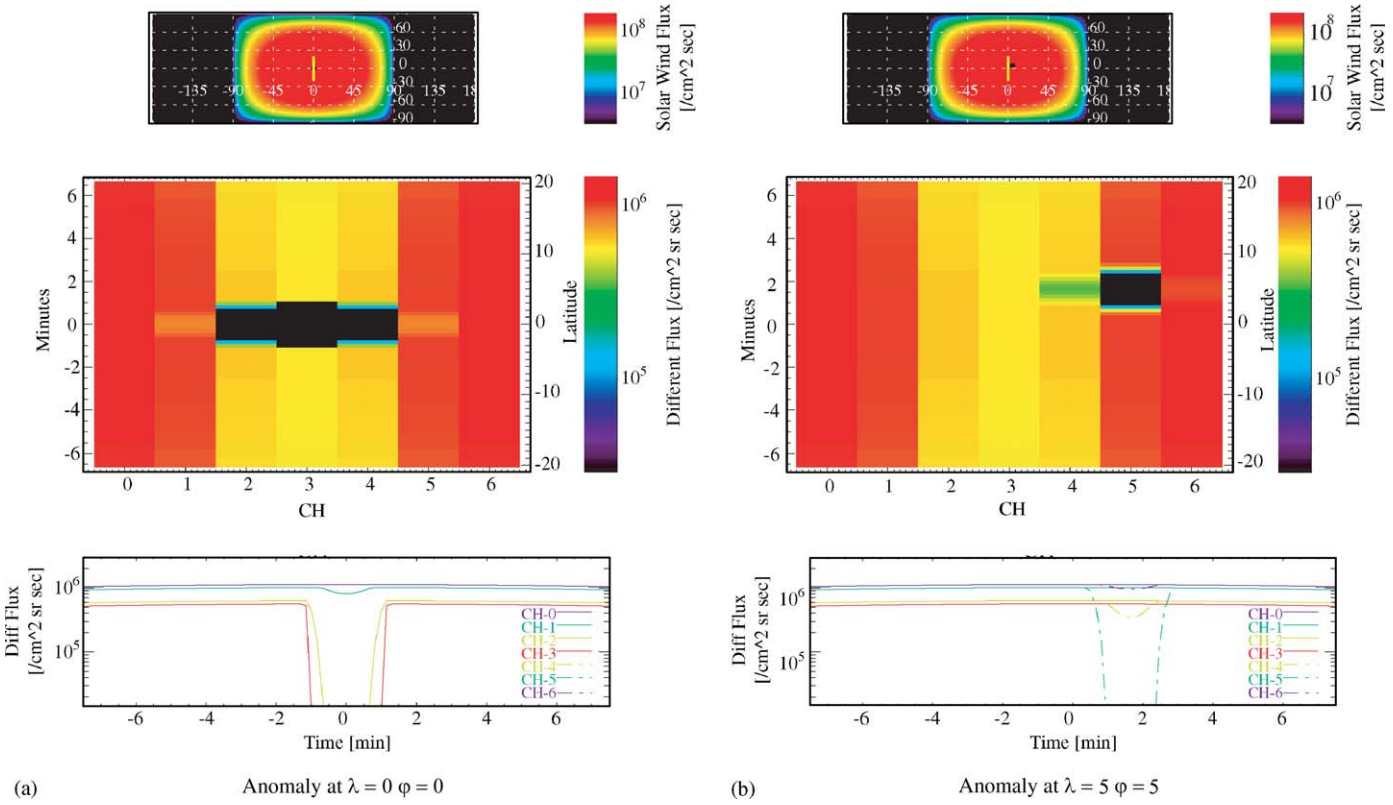

Fig. 8. Modeled solar wind flux (upper panels), images of expected oxygen flux measured (middle panels), and time series of the expected differential flux for each channels (lower panel). Magnetic anomalies are modeled by LENA flux depletion due to the protection of solar wind bombardment at the surface. Anomalies are located at (a) the sub-solar point, and (b) $\lambda = 5°$, $\phi = 5°$. The yellow lines show the satellite trajectory. It shows that a LENA imager can detect the existence of anomalies.

In both cases it is clearly seen that the magnetic anomalies are well depicted in the LENA images. LENA imaging of the magnetic anomalies will directly visualize the shape of the formed mini-magnetosphere. In other words, the LENA imaging can prove whether the existence of intense magnetic anomalies can stand-off the solar wind or not. Probably LENA imaging is the only global technique to study these miniature magnetospheres—the smallest known in the solar system.

The assumption used here is optimistic, but the solar wind flux is most likely to be modified by the small-scale magnetic anomalies. For example, Futaana et al. (2003) found the solar wind flux deflected by the local structure near the Moon.

LENA imaging of the same anomalies under various solar wind conditions may provide the dynamics of the mini-magnetosphere. For Earth's case, the magnetospheric dynamics can be described by fluid approximations; for example, its size changes mainly by the solar wind dynamic pressure (e.g. Sibeck et al., 1991). However, for Moon's case, kinetic effects are important. LENA imaging can provide valuable information for the comparable study of the magnetospheres.

3.4. Imaging of space weathering

Space weathering is the aggregate of the physical and chemical changes that occur to material exposed on the surface of an airless body. Micrometeorite bombardment, electromagnetic radiation, and particle sputtering are important factors changing the lunar regolith. Space weathering is of considerable interest for studies of surfaces since it causes major changes in the optical properties of the lunar surface. Space weathering is also an interesting topic for the planetary history. It is established in laboratory experiments that proton irradiation of loose powders results in their darkening and reddening (see an excellent review by Hapke (2001)).

We think LENA imaging can contribute to the study of the space weathering by the solar wind ion precipitation. As an example, we consider here swirl-like albedo structures (Hood et al., 1979; Richmond et al., 2003). These structures are sometimes found around the strong magnetic anomalies. Scientists have been trying to explain the coincidence of the two structures. One possible mechanism is the magnetic shielding hypothesis (e.g. Hood et al., 1979). Inside the magnetic anomalies the regolith is shielded from the solar wind flux while the surrounding areas receive a higher flux because of the formation of a mini-magnetosphere (Lin et al., 1998). Hood and Williams (1989) showed that the magnetic anomalies with magnitude of $B > 1000$ nT can significantly shield the solar wind flux. There are objections to this hypothesis. Because the solar wind flux cannot be shielded completely and the saturation time for the surface regolith is shorter enough compared to

the geologic times, more than 99.9% of the solar wind should be shielded by the magnetic anomalies. (e.g. Starukhina and Shkuratov, 2004).

Detailed image of sputtered LENAs can be converted to the detailed solar wind precipitation map at the lunar surface. Direct comparison of the precipitation map with optical or infrared images can be used for quantitative evaluation of the changes in the albedo and the total dose. It provides valuable clues to solve the open question of the coincidence between the magnetic anomaly and the space weathering.

4. Summary and conclusions

We have discussed topics of LENA-related lunar physics with simple theories and simulations. The calculations indicate that the sputtered LENA flux is high enough to be detected around the Moon for most of the main elements (O, Si, Al, Mg, Ca, Fe and Na). Therefore the imaging of the LENA can provide element maps of the sputtered particles from the lunar surface. The elemental maps should reflect the surface chemical composition.

The solar wind can penetrate into parts of the dark-areas because the solar wind protons have finite gyro-radius and the pressure gradient in the lunar wake area. By modeling the diffusion problem into the vacuum region, we obtained the amount of solar wind flux behind the terminator of the Moon, which depends only on the ion-acoustic Mach number. The formula shows that the nominal solar wind can reach up to 10° behind the terminator, i.e., LENAs can be generated within that angle in the dark hemisphere. We also modeled a crater at the pole and found that the bottom of the crater, i.e. a permanent shadowed region, is illuminated by the solar wind, and hence the LENAs can be generated from region inside crater.

LENA observations can see the interaction, if it exists, between the solar wind and lunar magnetic anomalies. This interaction is expected to form the mini-magnetosphere systems around large anomalies (e.g. Lin et al., 1998), and if so, the solar wind would be deflected around them producing LENA void regions that can be observed. The void regions represent the distribution of strong magnetic anomalies. It is a new technique to make lunar surface magnetic maps and this technique can be complemented by traditional magnetometer or electron reflectometer observations. Also, solar wind protons are one of the major sources of space weathering of the lunar surface materials, and the observation of lunar LENAs will provide new information on the evolutionary history of the lunar regolith.

Because the Moon has no global magnetic field and no dense atmosphere, the Moon–solar wind interactions are different from those of the Earth. Measurements of lunar LENAs provide us with many valuable perspectives about the physics not only on the Moon itself but also on other non-atmospheric bodies in the solar system, such as Mercury. Mercury has a weak intrinsic magnetosphere and hence is an obvious candidate where solar wind may directly interact with its surface. Actually, this is expected to happen when the dynamic pressure is enough high. In this case the interaction becomes similar to the Moon's case. The LENA observation around the Moon is a new appropriate tool for investigating bodies with thin atmosphere.

Acknowledgements

Y. Futaana is supported by Postdoctoral Fellowships for Research Abroad of the Japan Society for the Promotion of Science. A part of this research was performed while A. Bhardwaj was a National Research Council Senior Research Associate at NASA Marshall Space Flight Center. We thank Prof. R. Sridharan for encouragement and support.

References

Arnold, J.R., 1979. Ice in the lunar polar regions. J. Geophys. Res. 84, 5659–5668.

Barabash, S., Norberg, O., Lundin, R., Olsen, S., Lundin, K., Brandt, P.C., Roelof, E.C., Chase, C.J., Mauk, B.H., Koskinen, H., Rynö, J., 1998. Energetic neutral atom imager on the Swedish microsatellite Astrid. In: Pfaff, R.F., Borovsky, J.E., Young, D.T. (Eds.), Measurement Techniques in Space Plasmas, Field. AGU Geophysical Monograph, vol. 103. American Geophysical Union, Washington, DC, pp. 257–262.

Barabash, S., Lukyanov, A.V., Brandt, P.C., Lundin, R., 2001. Energetic neutral atom imaging of Mercury's magnetosphere 3. Simulated images and instrument requirements. Planet. Space Sci. 49, 1685–1692.

Barabash, S., Holmström, M., Lukyanov, A., Kallio, E., 2002. Energetic neutral atoms at Mars 4. Imaging of planetary oxygen. J. Geophys. Res. 107 (A10), 1280.

Baumjohann, W., Treumann, R.A., 1997. Basic Space Plasma Physics. Imperial College Press.

Betz, G., Wien, K., 1994. Energy and angular distributions of sputtered particles. Int. J. Mass Spectr. Ion Process. 140, 1–110.

Bhardwaj, A., Barabash, S., Futaana, Y., Kazama, Y., Asamura, K., McCann, D., Sridharan, R., Holmström, M., Wurz, P., Lundin, R., 2005. Low energy neutral atom imaging on the Moon with SARA instrument aboard Chandrayaan-1 mission. Journal of Earth System Science, 114, in press.

Birch, P.C., Chapman, S.C., 2001. Detailed structure and dynamics in particle-in-cell simulations of the lunar wake. Phys. Plasmas 8 (10), 4551–4559.

Bussey, D.B.J., Lucey, P.G., Steutel, D., Robinson, M.S., Spudis, P.D., Edwards, K.D., 2003. Permanent shadow in simple craters near the lunar poles. Geophys. Res. Lett. 30 (6), 1278, doi:10.1029/2002GL016180.

Colburn, D.S., Currie, R.G., Mihalov, J.D., Sonett, C.P., 1967. Diamagnetic solar-wind cavity discovered behind moon. Science 158, 1040–1042.

Crider, D.H., Vondrak, R.R., 2003. Space weathering effects on lunar cold trap deposits. J. Geophys. Res. 108 (E7) 5079, doi:10.1029/2002JE002030.

C:son Brandt, P., Barabash, S., Roelof, E.C., Chase, C.J., 2001. Energetic neutral atom imaging at low altitudes from the Swedish microsatellite Astrid: observations at low ($\leqslant$10 keV) energies. J. Geophys. Res. 106 (A11), 24,663–24,674.

Elphic, R.C., Funsten III, H.O., Barraclough, B.L., McComas, D.J., Paffett, M.T., Vaniman, D.T., Heiken, G., 1991. Lunar surface

composition and solar wind-induced secondary ion mass spectrometry. Geophys. Res. Lett. 18 (11), 2165–2168.
Feldman, P.D., Morrison, D., 1991. The Apollo 17 ultraviolet spectrometer: lunar atmosphere measurements revisited. Geophys. Res. Lett. 18 (11), 2105–2108.
Feldman, W.C., Maurice, S., Binder, A.B., Barraclough, B.L., Elphic, R.C., Lawrence, D.J., 1998. Fluxes of fast and epithermal neutrons from Lunar Prospector: evidence for water ice at the lunar poles. Science 281, 1496–1500.
Feldman, W.C., Lawrence, D.J., Elphic, R.C., Barraclough, B.L., Maurice, S., Genetay, I., Binder, A.B., 2000. Polar hydrogen deposits on the Moon. J. Geophys. Res. 105 (E2), 4175–4195.
Flynn, B., Mendillo, M., 1995. Simulations of the lunar sodium atmosphere. J. Geophys. Res. 100 (E11), 23,271–23,278.
Futaana, Y., Machida, S., Saito, Y., Matsuoka, A., Hayakawa, H., 2001. Conterstreaming electrons in the near vicinity of the Moon observed by plasma instruments on board NOZOMI. J. Geophys. Res. 106, 18,729–18,740.
Futaana, Y., Machida, S., Saito, Y., Matsuoka, Hayakawa, H., 2003. Moon-related nonthermal ions observed by Nozomi: species, sources, and generation mechanisms. J. Geophys. Res. 108 (A1), 1025, doi:10.1029/2002JA009366.
Hapke, B., 2001. Space weathering from Mercury to the asteroid belt. J. Geophys. Res. 106 (E5), 10,039–10,073.
Harnett, E.M., Winglee, R.M., 2002. 2.5D particle and MHD simulations of mini-magnetospheres at the Moon. J. Geophys. Res. 107 (A12), 1421, doi:10.1029/2002JA009241.
Henderson, M.G., Reeves, G.D., Spence, H.E., Sheldon, R.B., Jorgensen, A.M., Blake, J.B., Fennell, J.F., 1997. First energetic neutral atom images from Polar. Geophys. Res. Lett. 24 (10), 1167–1170.
Hilchenbach, M., Hovestadt, D., Klecker, B., Möbius, E., 1991. Detection of singly ionized energetic lunar pick-up ions upstream of Earth's bow shock. In: Marsch, E., Schwenn, G. (Eds.), Proceedings Solar Wind Seven, Pergamon Press, Oxford, pp. 349–355.
Hood, L.L., Williams, C.R., 1989. The lunar swirls: distribution and possible origins. Proceedings of the 19th Lunar Planetary Science Conference, pp. 99–113.
Hood, L.L., Coleman Jr., P.J., Wilhelms, D.E., 1979. The moon: sources of the crustal magnetic anomalies. Science 204, 53–57.
Johnson, R.E., 1989. Application of laboratory data to the sputtering of a planetary regolith. Icarus 78, 206–210.
Johnson, R.E., 1990. Energetic Charged-Particle Interactions with Atmospheres and Surfaces. Springer, Berlin.
Johnson, R.E., 2000. Sodium at Europa. Icarus 143, 429–433.
Johnson, R.E., Baragiola, R., 1991. Lunar surface: sputtering and secondary ion mass spectrometry. Geophys. Res. Lett. 18 (11), 2169–2172.
Johnson, J.R., Feldman, W.C., Lawrence, D.J., Maurice, S., Swindle, T.D., Lucey, P.G., 2002a. Lunar Prospector epithermal neutrons from impact craters and landing sites: implications for surface maturity and hydrogen distribution. J. Geophys. Res. 107 (E2), 5008, doi:10.1029/2000JE001430.
Johnson, R.E., Leblanc, F., Yakshinskiy, B.V., Madey, T.E., 2002b. Energy distributions for desorption of sodium and potassium from ice: the Na/K ratio at Europa. Icarus 156, 136–142.
Kazama, Y., Barabash, S., Bhardwaj, A., Asamura, K., Futaana, Y., Holmström, M., Lundin, R., Sridharan, R., Wurz, P. Energetic neutral atom imaging mass spectroscopy of the moon and mercury environments. Adv. Space Res., in press.
Lammer, H., Wurz, P., Patel, M.R., Killen, R., Kolb, C., Massetti, S., Orsini, S., Milillo, A., 2003. The variability of mercury's exosphere by particle and radiation induced surface release processes. Icarus 166 (2), 238–247.
Lin, R.P., Mitchell, D.L., Curtis, D.W., Anderson, K.A., Carlson, C.W., McFadden, J., Acuña, M.H., Hood, L.L., Binder, A., 1998. Lunar surface magnetic fields and their interaction with the solar wind: results from Lunar Prospector. Science 281, 1480–1484.
Mall, U., Kirsch, E., Cierpka, K., Wilken, B., Söding, A., Neubauer, F., Gloeckler, G., Galvin, A., 1998. Direct observation of lunar pick-up ions near the Moon. Geophys. Res. Lett. 25 (20), 3799–3802.
Managadze, G.G., Sagdeev, R.Z., 1988. Chemical composition of small bodies of the solar system determined from the effects of solar-wind interaction with their surfaces. Icarus 73, 294–302.
Mauk, B.H., Mitchell, D.G., Krimigis, S.M., Roelof, E.C., Paranicas, C.P., 2003. Energetic neutral atoms from a trans-Europa gas torus at Jupiter. Nature 421, 920–922.
Mitchell, D.G., Jaskulek, S.E., Schlemm, C.E., Keath, E.P., Thompson, R.E., Tossman, B.E., Boldt, J.D., Hayes, J.R., Andrews, G.B., Paschalidis, N., Hamilton, D.C., Lundgren, R.A., Tums, E.O., Wilson IV, P., Voss, H.D., Prentice, D., Hsieh, K.C., Curtis, C.C., Powell, F.R., 2000. High energy neutral atom (HENA) imager for the IMAGE mission. Space Sci. Rev. 91 (1–2), 67–112.
Moore, T.E., Chornay, D.J., Collier, M.R., Herrero, F.A., Johnson, J., Johnson, M.A., Keller, J.W., Laudadio, J.F., Lobell, J.F., Ogilvie, K.W., Rozmarynowski, P., Fuselier, S.A., Ghielmetti, A.G., Hertzberg, E., Hamilton, D.C., Lundgren, R., Wilson, P., Walpole, P., Stephen, T.M., Peko, B.L., Van Zyl, B., Wurz, P., Quinn, J.M., Wilson, G.R., 2000. The low energy neutral atom imager for IMAGE. Space Sci. Rev. 91 (1–2), 155–195.
Morgan, T.H., Killen, R.M., 1997. A non-stoichiometric model of the composition of the atmosphere of Mercury and the Moon. Planet. Space Sci. 45 (1), 81–94.
Ogilvie, K.W., Steinberg, J.T., Fitzenreiter, R.J., Owen, C.J., Lazarus, A.J., Farrell, W.M., Torbert, R.B., 1996. Observation of the lunar plasma wake from the WIND spacecraft on December 27, 1994. Geophys. Res. Lett. 23 (10), 1255–1258.
Pollock, C.J., Asamura, K., Baldonado, J., Balkey, M.M., Barker, P., Burch, J.L., Korpela, E.J., Cravens, J., Dirks, G., Fok, M.-C., Funsten, H.O., Grande, M., Gruntman, M., Hanley, J., Jahn, J.-M., Jenkins, M., Lampton, M., Marckwordt, M., McComas, D.J., Mukai, T., Penegor, G., Pope, S., Ritzau, S., Schattenburg, M.L., Scime, E., Skoug, R., Spurgeon, W., Stecklein, T., Storms, S., Urdiales, C., Valek, P., van Beek, J.T.M., Weidner, S.E., Wüest, M., Young, M.K., Zinsmeyer, C., 2000. Medium energy neutral atom (MENA) imager for the IMAGE mission. Space Sci. Rev. 91 (1–2), 113–154.
Potter, A.E., Morgan, T.H., 1988. Extended sodium exosphere of the Moon. Geophys. Res. Lett. 15 (13), 1515–1518.
Richmond, N.C., Hood, L.L., Halekas, J.S., Mitchell, D.L., Lin, R.P., Acuña, M., Binder, A.B., 2003. Correlation of a strong lunar magnetic anomaly with a high-albedo region of the Descartes mountains. Geophys. Res. Lett. 30 (7), 1395, doi:10.1029/2003GL016938.
Russell, C.T., Lichtenstein, B.R., 1975. On the source of lunar limb compressions. J. Geophys. Res. 80 (34), 4700–4711.
Samir, U., Write Jr., K.H., Stone, N.H., 1983. The expansion of a plasma into a vacuum: basic phenomena and processes and applications to space plasma physics. Rev. Geophys. Space Phys. 21, 1631–1646.
Sibeck, D.G., Lopez, R.E., Roelof, E.C., 1991. Solar wind control of the magnetopause shape, location and motion. J. Geophys. Res. 96 (A4), 5489–5495.
Sigmund, P., 1969. Theory of sputtering. I. sputtering yield of amorphous and polycrystalline targets. Phys. Rev. 184, 383–416.
Sprague, A.L., Kozlowski, R.W.H., Hunten, D.M., Wells, W.K., Grosse, F.A., 1992. The sodium and potassium atmosphere of the Moon and its interaction with the surface. Icarus 96, 27–42.
Starukhina, L.V., Shkuratov, Y.G., 2004. Swirls on the Moon and Mercury: meteoroid swarm encounters as a formation mechanism. Icarus 167, 136–147.
Thompson, M.W.I., 1968. The energy spectrum of ejected atoms during the high energy sputtering of gold. Philos. Mag. 18, 377–414.
Wiens, R.C., Burnett, D.S., Calaway, W.F., Hansen, C.S., Lykke, K.R., Pellin, M.J., 1997. Sputtering products of sodium sulfate: implications for Io's surface and for sodium-bearing molecules in the Io torus. Icarus 128, 386–397.
Wurz, P., Lammer, H., 2003. Monte-Carlo simulation of Mercury's exosphere. Icarus 1641 (1), 1–13.